^{12}C(p, p′)^{12}C Reaction (E_p = 19.5–30 MeV) for Active Interrogation of Special Nuclear Material

J. Nattress[1,2,*] F. Sutanto,[1] P.-W. Fang,[3] Y.-Z. Chen,[3] A. Cheng,[3] K.-Y. Chu,[4] T.-S. Duh,[4]
H.-Y. Tsai,[3] M.-W. Lin,[3,†] and I. Jovanovic[1]

[1]*Department of Nuclear Engineering and Radiological Sciences, University of Michigan, Ann Arbor,
Michigan 48109, USA*
[2]*Oak Ridge National Laboratory, Oak Ridge, Tennessee 37830, USA*
[3]*Institute of Nuclear Engineering and Science, National Tsing Hua University, Hsinchu 30013, Taiwan*
[4]*Isotope Application Division, Institute of Nuclear Energy Research, Taoyuan City 32546, Taiwan*

Passive detection of special nuclear material (SNM) is challenging due to its inherently low rate of spontaneous emission of penetrating radiation, the relative ease of shielding, and the fluctuating and frequently overwhelming background. Active interrogation, the use of external radiation to increase the emission rate of characteristic radiation from SNM, has long been considered to be a promising method to overcome those challenges. Current active-interrogation systems that incorporate radiography tend to use bremsstrahlung beams, which can deliver high radiation doses. Low-energy ion-driven nuclear reactions that produce multiple monoenergetic photons may be used as an alternative. The ^{12}C(p, p′)^{12}C reaction is one such reaction that could produce large yields of highly penetrating 4.4- and 15.1-MeV gamma rays. This reaction does not directly produce neutrons below the approximately 19.7 MeV threshold, and the 15.1-MeV gamma-ray line is well matched to the photofission cross section of ^{235}U and ^{238}U. We report the measurements of thick-target gamma-ray yields at 4.4 and 15.1 MeV from the ^{12}C(p, p′)^{12}C reaction at proton energies of 19.5, 25, and 30 MeV. Measurements are made with two 3-in. EJ-309 cylindrical liquid scintillation detectors and thermoluminescent dosimeters placed at 0° and 90°, with an additional 1.5-in. NaI(Tl) cylindrical scintillation detector at 0°. We estimate the highest yields of the 4.4- and 15.1-MeV gamma rays of 1.65×10^{10} and 4.47×10^8 sr^{-1} μC^{-1} at a proton energy of 30 MeV, respectively. The yields in all experimental configurations are greater than in a comparable deuteron-driven reaction that produces the same gamma-ray energies—^{11}B(d, nγ)^{12}C. However, a significant increase of the neutron radiation dose accompanies the proton energy increase from 19.5 to 30 MeV.

I. INTRODUCTION

Screening and interdiction of shielded special nuclear material (SNM) is a significant nuclear-security concern. The problem encompasses not only cargo containers but also smaller objects, as well as the movement of illicit materials into and out of enrichment facilities [1,2]. Several million ocean cargo containers arrive at U.S. seaports annually [3,4], with more than half the distribution concentrated at three ports—Los Angeles, Long Beach, and New York [3]. The large traffic and its uneven distribution raise serious concerns about the number of containers that can be accurately scanned without

impeding commerce and still maintaining nuclear-security vigilance.

The technique of active interrogation has been of increasing interest in recent years for detecting SNM [5]. This is based on an expectation that the increased magnitude and the time structure of the fission signatures imposed by active interrogation can increase the probability of SNM detection. Innovative approaches are needed to overcome specific application constraints, such as the maximum scanning time and radiation dose. Traditional active-interrogation systems tend to use energetic-x-ray transmission radiography using continuous-energy-spectrum bremsstrahlung beams. Such beams can deliver high radiation doses, especially at the high electron energies needed to produce sufficiently energetic photons for penetrating radiography and to induce photofission. The lower-energy photons in the

*nattressjt@ornl.gov
†mwlin@mx.nthu.edu.tw

bremsstrahlung spectrum, well below the photofission threshold, have low penetration through objects with high areal density and may significantly contribute to the imparted radiation dose while not inducing fission [6,7].

Low-energy ion-driven nuclear reactions that produce multiple monoenergetic, high-energy gamma rays could be used as an alternative to bremsstrahlung in active-interrogation applications. Reactions that exhibit a large positive Q value allow the use of lower-energy (and thus typically smaller and simpler) accelerators to create highly penetrating energetic photons. Such monoenergetic or multiple-monoenergetic sources may offer benefits such as improved performance in radiography and higher fission rates per unit of imparted radiation dose. Near-monoenergetic photon sources at or near the photofission resonance (approximately 15 MeV) offer a factor of 4 lower imparted radiation dose when compared with a bremsstrahlung source with a 19-MeV endpoint energy [6]. Low-energy nuclear reactions, therefore, are a promising method to produce quasimonoenergetic photon beams that could lead to the construction of lower-dose, small-footprint systems to detect illicit movement of SNM as well as support a broad range of measurements in the area of nuclear security, nuclear nonproliferation, and nuclear safety.

Figure 1 provides a conceptual design of one specific application—a cargo-screening active-interrogation system—where a low-energy nuclear-reaction source could be used to increase the scanning rate by implement ion of simultaneous scanning of multiple cargo streams. Such a system would need to address some of the major specifications for cargo-container scanning, including an acceptable radiation dose imparted to the cargo, penetration capability, container-scanning speed, and material-discrimination performance [8].

Several candidate reactions have been identified that produce prolific yields of energetic gamma rays, including those above the photofission energy threshold, or neutrons that may also be viable for active interrogation [10]. Such high-energy particles can be used to penetrate dense cargo to perform transmission radiography for material identification [11–13] or induce fission [14,15]. In Ref. [10] several candidate reactions were considered, including (p,γ), (p,$\alpha\gamma$), and (d,nγ). Four candidate targets (^{11}B, ^{7}Li, ^{19}F, and ^{15}N) were selected on the basis of the reaction Q values and gamma-ray energies from the daughter excited nuclei. Protons, deuterons, and tritons were used as projectiles. The ^{11}B(d, n)^{12}C reaction ($Q = 13.6$ MeV) has emerged as one of the leading candidates for an active-interrogation source [16]. With deuteron energies of several million electronvolts or higher, this reaction produces a strong 15.1-MeV gamma-ray energy line that is well overlapped with the photofission cross section of ^{235}U and ^{238}U [17]. This reaction, however, has a high neutron
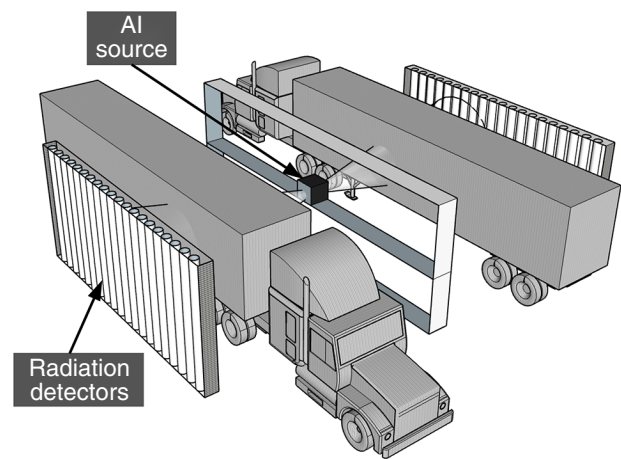

FIG. 1. Conceptual design of a cargo-scanning system using a low-energy nuclear-reaction-based active-interrogation source. A single source may be used to implement simultaneous scanning of multiple cargo streams [9].

yield, approximately 20–50 times the relevant gamma-ray yield [11].

With the continued advancement of superconducting cyclotron technology, more-compact, deployable active-interrogation systems using nuclear reactions that do not directly produce neutrons can be envisioned. One such reaction that can excite the 15.1-MeV state of ^{12}C inelastically is the ^{12}C(p, p')^{12}C reaction [18–21]. This reaction has an incident-proton threshold energy of 16.39 MeV for exciting the 15.1-MeV ^{12}C state and does not directly produce neutrons below the approximately 19.6 MeV threshold [22,23]. Gamma rays at 4.4 MeV are also produced prolifically in this reaction, and can be used in conjunction with 15.1-MeV gamma rays to perform spectroscopic transmission radiography and identify the atomic number of an unknown material [11,12].

Organic scintillation detectors are typically used to perform fast neutron spectroscopy, where pulse-shape analysis enables the discrimination between neutrons and photons. While it is well known that low-Z organic scintillators are also sensitive to photons and their response is nearly proportional, photon spectroscopy is usually not attempted due to low efficiency, low resolution, and the absence of photopeak features in the light-output spectrum. Although the presence of prominent full-energy deposition peaks is often favored for photon spectroscopy, many common high-Z scintillators depend on expensive crystalline materials with slow-decay timing characteristics, which perform poorly in high-rate environments. They can also be costly to scale to large volumes, or may not be able to distinguish between neutron and photon interactions. The fast rise-time and decay-time response of an organic liquid scintillator, along with the ability to detect

and identify both neutrons and photons, makes it an attractive choice for an active-interrogation system that requires simultaneous photon and neutron identification in a mixed-radiation, high-rate environment. If the photon source has a spectrum that features well-separated discrete energies, discernible spectral features can be observed in the resulting light-output spectrum, which can be used to perform spectroscopy [24].

We present gamma-ray yield measurements of the ^{12}C(p, p')^{12}C reaction made with two organic liquid scintillators placed at 0° and 90° with respect to the proton-beam axis, with an additional Na(Tl) detector placed at 0° for experimental validation. We further report neutron and gamma-ray dose measurements. We observe an increase in the production rate of gamma rays with an increase in proton energy, as well as a rapid increase in the measured neutron radiation dose with proton energy. The active-interrogation source proposed in this work focuses on the key performance parameters—the emitted radiation flux, energy spectrum, and dose rate. Other essential design considerations, such as radiation-shielding requirements, must be considered before final implementation.

II. MATERIALS AND METHODS

The experiments are conducted with a cyclotron located at the Institute of Nuclear Energy Research in Taiwan. This accelerator produces proton pulses at a fixed frequency of 73.2 MHz, and the proton energy can be adjusted from 15 to 30 MeV with a maximum average current of $10\,\mu$A delivered to the experimental station. A 6.35-mm-thick natural carbon target consisting of 98.9% ^{12}C and 1.1% ^{13}C and an active area of 2×2 cm^2 is held by an aluminum mount and placed at the center of an aluminum vacuum chamber ($20 \times 20 \times 20$ cm^3, 1.2 cm thick). To prevent protons from striking the target mount and generating neutrons at the target location, a 1-cm-thick aluminum collimator is inserted into the upstream beamline to shape the incident proton beam to a transverse diameter of 1 cm before it enters the target chamber. This collimation, however, inevitably produces additional neutrons when protons in the outer radial region of each pulse strike the aluminum collimator. Therefore, a water tank ($1 \times 1 \times 1$ m^3) is placed to surround the vacuum pipe to shield it from neutrons emitted from the collimator. The on-target proton current is calibrated when the target mount is replaced by a Faraday cup, whose output is connected to a digital
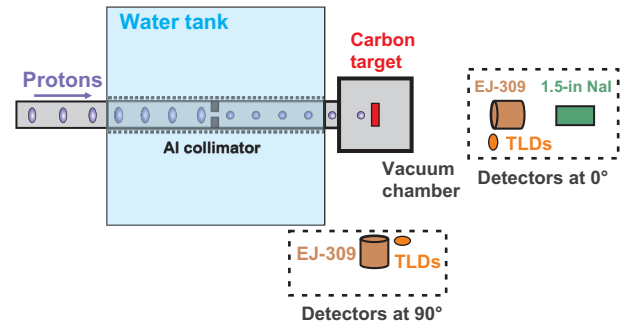

FIG. 2. The experimental setup.

picoammeter (Keithley, model 486) with a resolution of 10 fA.

The radiation produced by the source is measured with one NaI(Tl) scintillation detector, two EJ-309 organic liquid scintillation detectors [25], and pairs of thermoluminescent dosimeters (TLDs). The NaI(Tl) detector is placed at 0° at a distance of 2.05 m from the carbon target, while the EJ-309 liquid scintillation detectors and TLDs are placed at 0° and 90°, at the same distance of 1.4 m. Here the angles are given with respect to the propagation axis of protons incident on the target. The diameter and the height of the NaI(Tl) detector are both 1.5 in. and the diameter and the height of the EJ-309 detectors are both 3 in. The smaller NaI(Tl) detector is selected to minimize pileup and provide relatively clean photon spectra to validate the findings obtained with the organic scintillators.

Figure 2 shows a diagram of the experimental setup, including the aluminum collimator, vacuum target chamber, water tank for neutron shielding, one NaI(Tl) scintillation detector, two EJ-309 liquid scintillators, and two paired TLDs. Table I summarizes the positions and solid angles subtended by the detectors, as measured relative to the target. The detectors are placed at nearly the same heights as the target height (1.5 m above the ground level). Three proton-projectile-target configurations are tested. The compact superconducting cyclotron is operated at on-target currents of 0.35, 0.3, and 0.33 nA with proton energies of 19.5, 25, and 30 MeV incident on the carbon target, respectively. At each proton energy, data are recorded for 8 h.

Signals generated by the scintillation detectors are digitized by an eight-channel, 14-bit, 500-MHz waveform digitizer (CAEN DT5730) with a 992-ns-long waveform record. CAEN Multi-PArameter Spectroscopy Software

TABLE I. Summary of characteristics of the scintillation detectors and their placement relative to the target.

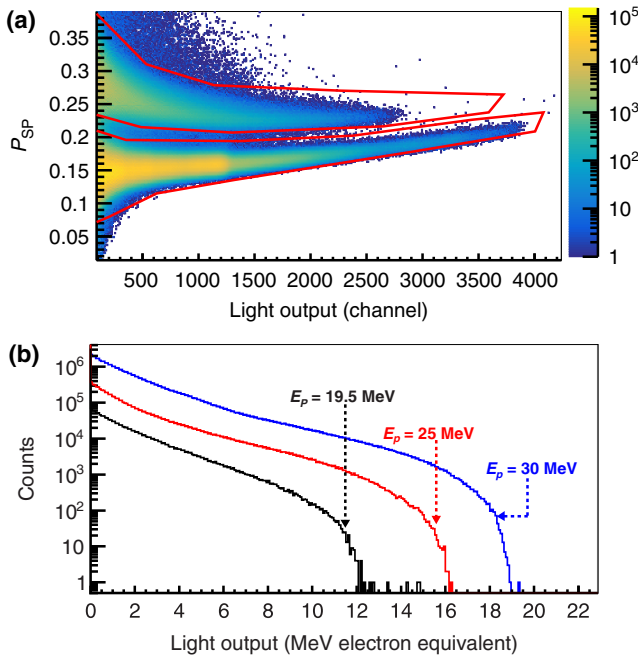| Angle (deg)	Detector	Radial distance (m)	Height (m)	Solid angle (sr)
0	1.5×1.5 in.^{2} NaI(Tl)	2.05	1.53	2.7×10^{-4}
	3×3 in.^{2} EJ-309	1.4	1.45	2.3×10^{-3}
90	3×3 in.^{2} EJ-309	1.4	1.2	2.3×10^{-3}

FIG. 3. (a) Response of a 3-in. EJ-309 detector for 19.5-MeV protons with the neutron (higher P_{SP}) and photon (lower P_{SP}) fiducial cuts shown in red and (b) the neutron light-output response for 19.5-, 25-, and 30-MeV protons incident on a natural carbon target for a measurement time of 8 h.

(CoMPASS) [26] is used to record the integrated charge in two distinct time windows measured with respect to the pulse trigger. We refer to these two recorded quantities as the "long-gate integral'" (Q_{long}) and the "short-gate integral" (Q_{short}). Pulse-shape analysis is performed with the digitizer field-programmable gate array by calculation of the pulse-shape parameter (P_{SP}) for each signal waveform, which is defined as

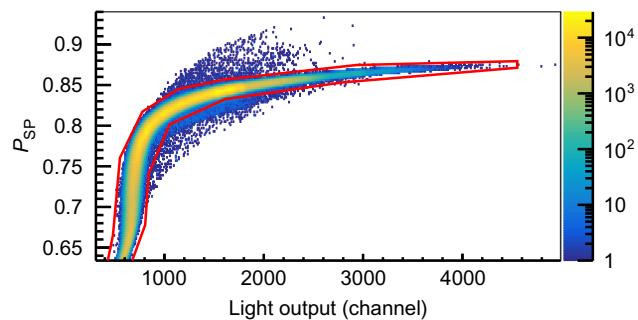$$P_{SP} = \left(Q_{long} - Q_{short}\right) / Q_{long}. \tag{1}$$

FIG. 4. Response of a 1.5-in. NaI(Tl) detector for 19.5-MeV protons incident on a natural carbon target for a measurement time of 8 h. The photon fiducial cut is shown in red.

For the NaI(Tl) detector, Q_{long} and Q_{short} are defined as the total charge in the time windows [t_s, $t_s + 400$ ns] and [t_s, $t_s + 100$ ns], respectively, with the reference delay $t_s = 50$ ns after the leading-edge trigger. The time windows for the EJ-309 detectors are [$t_s + 400$ ns] and [$t_s + 54$ ns] for Q_{long} and Q_{short}, respectively, where the trigger delay is set to $t_s = 10$ ns. By our performing the fiducial cut in the P_{SP}–light-output parameter space of the response of the EJ-309 detectors, single-photon events can be distinguished from both neutron and pileup events. A P_{SP}–light-output scatter plot with the fiducial cuts (red) for one of the EJ-309 detectors and the NaI(Tl) detector is shown in Figs. 3 and 4. Also in Fig. 3, the neutron light-output response for 19.5-, 25-, and 30-MeV protons incident on a natural carbon target is shown, indicating an increase in neutron energy with increasing incident proton energy. Table. II summarizes the observed event rates over the 8-h measurement time. The 3-in. EJ-309 detector at 0° exhibits the highest event rate in each experiment. Meanwhile, the EJ-309 detector at 90° and the NaI(Tl) detector at 0° experience lower event rates (approximately 60% and approximately 10% of the rates for the EJ-309 detector at 0°, respectively). According to the time stamps recorded by the digitizer, the dead time of the detection system is calculated to be approximately $1.024\,\mu s$; therefore, the true counting rates are estimated according to the nonparalyzable model [27], and are listed in Table II.

Fiducial cuts are used to select photon events and reject pileup events, and events within the respective cuts are used to produce the photon light-output distributions for each detector for three proton-projectile-target experimental configurations. Figure 5 shows a representative photon light-output distribution that corresponds to the response of the EJ-309 detector at 90° for a proton energy of 25 MeV.

In Fig. 5 the double-escape peaks from 4.4- and 15.1-MeV gamma rays are readily observable, along with the Compton-scattering feature at 4.4 MeV [24]. As expected, there is no observable photopeak due to the low

TABLE II. Summary of the observed counting rates and estimated true counting rates.

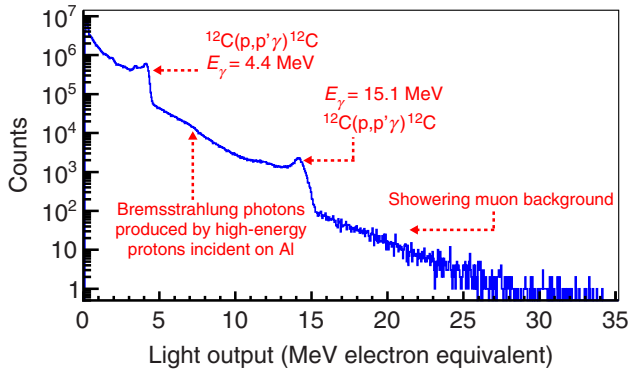| Detector	Proton energy	Counting rate	
	(MeV)	Observed (kHz)	True (kHz)
EJ-309, 0°	19.5	2.823	2.831
	25	7.6	7.656
	30	27.013	27.782
EJ-309, 90°	19.5	1.92	1.923
	25	4.902	4.927
	30	15.821	16.082
NaI, 0°	19.5	0.376	0.376
	25	0.943	0.944
	30	2.81	2.818

FIG. 5. Recorded light-output spectrum measured with a 3-in. EJ-309 detector detector at 90° over a measurement time of 8 h for a proton energy of 25 MeV incident on a natural carbon target.

atomic numbers of the liquid scintillation detector's constituents. The broad energy distribution at high light output (greater than or equal to 20 MeV electron equivalent) is attributed to muon energy loss in the detector volume. The continuum between the 4.4- and 15.1-MeV spectral features is attributed to bremsstrahlung produced by high-energy protons incident on the aluminum collimator placed upstream of the target; this is corroborated by simulation as discussed in Sec. III.

Photon and neutron radiation doses at 0° and 90° are measured for 8 h and are distinguished from each other on the basis of on the dual-TLD method [28]. In this method, pairs of TLD-600 and TLD-700 chips ($3.2 \times 3.2 \times 0.89$ mm³, Harshaw) are placed 1.4 m from the carbon target at each angle. The TLD-700 chip is primarily sensitive to photons, since 99.993% of its lithium-isotope content is ^{7}Li, which exhibits a much lower neutron response than that of ^{6}Li. In contrast, the 95.62% enrichment of ^{6}Li in the TLD-600 chip allows it to record the dose contributed by both neutrons and photons. By our placing paired TLDs in a mixed photon-neutron field, the TLD-600 reading Q_6 accounts for the majority of neutron-response reading $Q_{6,n}$ and the minority of photon-response reading $Q_{6,p}$, while the TLD-700 reading Q_7 is dominated by the photon-response reading $Q_{7,p}$ when compared with the neutron-response reading $Q_{7,n}$.

In our experiments, the total readings Q_6 and Q_7 measured at a given proton energy are averaged from three TLD chips of each type placed at each angle, which also allows consistency checks. When the TLD-600 and TLD-700 chips are placed at the same position, the measured $Q_{6,p}$ and $Q_{7,p}$ represent the same photon dose. This photon dose D_{ph} can be calibrated as

$$D_{\text{ph}} = Q_{x,p} \times C_{x,p}, \tag{2}$$

TABLE III. Yield of 4.4-MeV gamma-rays measured with the 3-in. EJ-309 detector.

Proton energy (MeV)	Angle (deg)	Yield (sr⁻¹ μC⁻¹)
19.5	0	$2.44 \times 10^9 \pm 6.1 \times 10^8$
	90	$2.12 \times 10^9 \pm 9.3 \times 10^8$
25	0	$6.07 \times 10^9 \pm 1.5 \times 10^9$
	90	$5.91 \times 10^9 \pm 2.6 \times 10^9$
30	0	$1.69 \times 10^{10} \pm 4.2 \times 10^9$
	90	$1.77 \times 10^{10} \pm 7.8 \times 10^9$

where $C_{x,p}$ stands for the calibration factor and $x = \{6, 7\}$ relates to the TLD-600 chip and the TLD-700 chip, respectively. These calibration factors are measured to be $C_{6,p} \sim 1.8 \times 10^{-5}$ mGy/nC and $C_{7,p} \sim 1.6 \times 10^{-5}$ mGy/nC with the ^{137}Cs field established in a dedicated calibration setup. Once the photon dose D_{ph} is determined from the TLD-700 measurements, the photon response $Q_{6,p}$ of the TLD-600 chip included in the total reading Q_6 can be estimated by

$$Q_{6,p} = D_{\text{ph}}/C_{6,p}, \tag{3}$$

since the TLD-600 chip experiences the same D_{ph} as the paired TLD-700 chip. As a result, the neutron-response reading $Q_{6,n}$ of the TLD-600 chip is determined from

$$Q_{6,n} = Q_6 - Q_{6,p}. \tag{4}$$

The TLD-600 chips are calibrated with use of a ^{252}Cf source, yielding $C_{H,n} \sim 1.7 \times 10^{-4}$ mSv/nC, which relates the neutron response $Q_{6,n}$ to the neutron-dose equivalent H_n (mSv):

$$H_n = C_{H,n} \times Q_{6,n}. \tag{5}$$

III. LIGHT-OUTPUT-SPECTRUM SIMULATION

Monte Carlo simulations are performed with GEANT4 10.3 [29] to help assess the spectral features in the recorded photon light-output distributions. The physics list QGSP_BERT_HP is used to model the particle interactions. The model includes the carbon target, the vacuum chamber, the collimator, the water tank, and the surrounding concrete wall; in this way, the effect of shielding and

TABLE IV. Yield of 15.1-MeV gamma rays measured with the 3-in. EJ-309 detector.

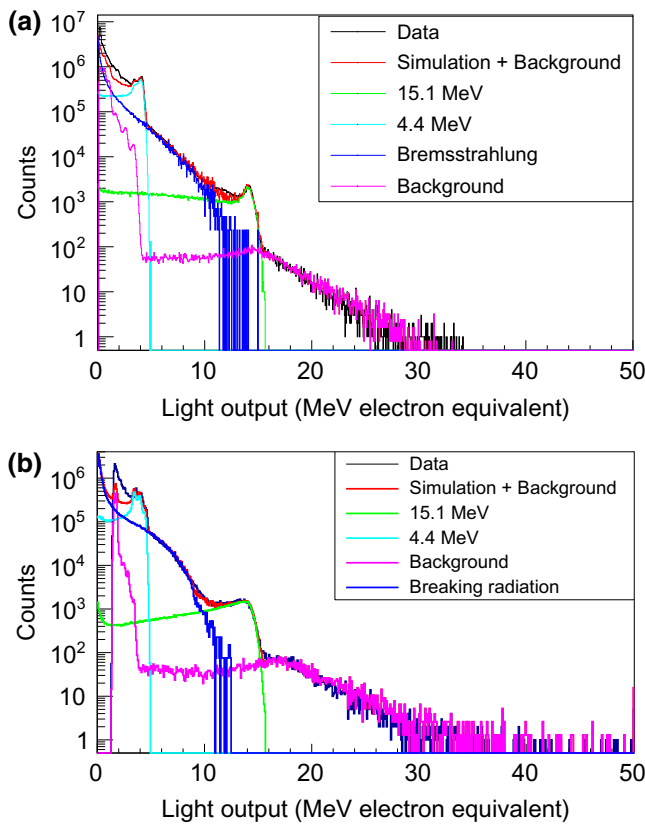| Proton energy (MeV)	Angle (deg)	Yield (sr⁻¹ μC⁻¹)
19.5	0	$9.38 \times 10^6 \pm 2.3 \times 10^6$
	90	$3.02 \times 10^7 \pm 1.3 \times 10^7$
25	0	$9.91 \times 10^7 \pm 2.5 \times 10^7$
	90	$1.58 \times 10^8 \pm 7.0 \times 10^7$
30	0	$2.06 \times 10^8 \pm 5.1 \times 10^7$
	90	$5.37 \times 10^8 \pm 2.4 \times 10^8$

FIG. 6. Experimental light output and simulated contributions to light output for (a) a 3-in. EJ-309 detector at 90° and (b) a 1.5-in. NaI(Tl) detector at 0° for 25-MeV protons incident on a thick natural carbon target over a measurement time of 8 h.

FIG. 7. Recorded light-output spectra measured with (a) a 3-in. EJ-309 detector detector at 90° and (b) a 1.5-in. NaI(Tl) detector at 0° for 25-MeV protons incident on a thick natural carbon target over a measurement time of 8 h.

the production of bremsstrahlung can be investigated and applied when the experimental results are being analyzed.

To investigate the continuum observed in the 5–10-MeV energy range, a simulation of high-energy proton interactions in a 1-cm-thick aluminum slab is performed. Bremsstrahlung photons propagate through the water tank and their energies are tallied. The softened spectrum is then used to sample the energy of a new group of photons, for which the direction of propagation is biased toward the detector. The simulated detector response to bremsstrahlung is obtained and smeared with the resolution function. The resolution is parameterized as outlined in Ref. [24]. Monte Carlo simulations of high-energy gamma-ray (4.4 and 15.1 MeV) interactions in the EJ-309 detectors are also performed to obtain the responses of individual detectors used in the experiments.

To calculate the gamma-ray yields at 4.4 and 15.1 MeV, four individual spectrum— measured background, simulated response to bremsstrahlung at the respective proton energy, and the simulated responses to 4.4- and 15.1-MeV photons—are fit to the measured data. A χ^2 analysis is used to determine the parameters that maximize the agree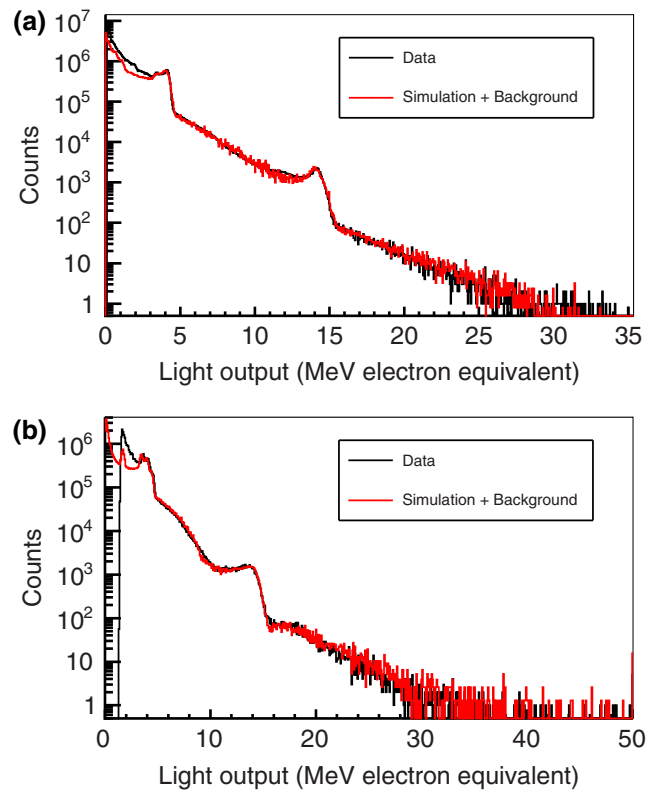ment between the measured detector response and the simulated detector responses. Local function minimization is performed with the MIGRAD, HESSE, and MINOS algorithms as implemented in the ROOT framework [30]. This analysis is conducted for each detector at each of the three proton energies. The resulting fit spectra are used to calculate the yields of 4.4- and 15.1-MeV gamma rays normalized to the solid angle and measured cyclotron current. The gamma-ray yields measured with the EJ-309 detectors are reported in Table III (4.4 MeV) and Table IV (15.1 MeV), with the NaI(Tl) detector producing results similar to the EJ-309 detector at 0°.

The simulated EJ-309 light-output responses to 4.4-MeV gamma rays, 15.1-MeV gamma rays, and bremsstrahlung are scaled and added to the background spectrum such that their sum matches the experimental light-output response. Individual contributions to the simulated spectrum, the combined simulated spectra, and the experimental spectra for the EJ-309 detector at 90° and the NaI(Tl) detector at 0° are shown in Fig. 6. In this example, protons ($E_p = 25$ MeV) are incident on a thick natural carbon target over a measurement time of 8 h.

The final combined fit for one of the experimental configurations for the NaI(Tl) detector and the EJ-309 detector
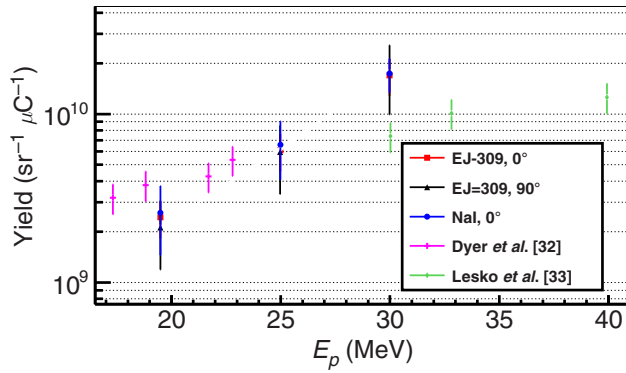
FIG. 8. Yields of 4.4-MeV gamma rays for the EJ-309 detectors and the NaI(Tl) detector at proton energies of 19.5, 25, and 30 MeV.

FIG. 9. Yields of 15.1-MeV gamma rays for the EJ-309 detectors and the NaI(Tl) detector for proton energies of 19.5, 25, and 30 MeV.

is shown in Fig. 7. The fit spectra show good agreement over the broad light-output range of interest.

By calculating the area under the simulated detector response for the individual contributions of 15.1- and 4.4-MeV gamma rays and knowing the on-target current used during the experiment and the experimental measurement time, we obtain the absolute detection efficiency from the simulation, and assuming an isotropic angular photon distribution, we estimate the production rates of 4.4- and 15.1-MeV gamma rays. Pileup corrections are applied to the production yields in accordance with the values listed in Table II. Because of unidentifiable sources of uncertainty in our measurements such as proton energy and time-varying backgrounds, a conservative approach to estimate the uncertainty is pursued. The bin errors of the measured light-output spectra were varied to achieve $\chi^2/N = 1$ for each measurement. The bin errors range from approximately 20% to 40%.

IV. RESULTS AND DISCUSSION

The results show an expected trend: as the energy of the protons is increased, the yield of high-energy gamma rays increases. The yields of 15.1-MeV gamma rays $(\mathrm{sr}^{-1}\,\mu\mathrm{C}\,\mathrm{s}^{-1})$ at 0° from the ^{12}C(p, p′)^{12}C reaction are factors of 1.3, 14.8, and 55.5 greater at proton energies of 19.5, 25, and 30 MeV, respectively, than the yield of
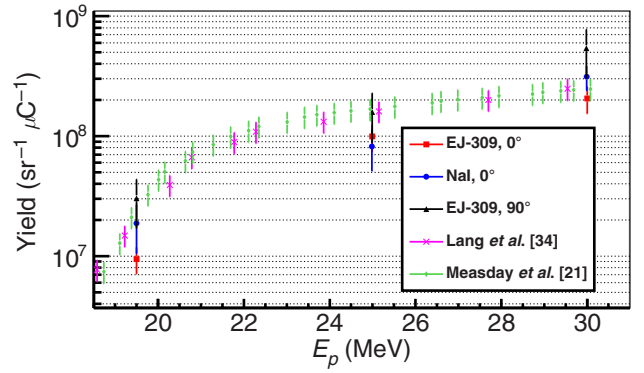
15.1-MeV gamma rays from the ^{11}B(d,n)^{12}C reaction at 0° with 3-MeV deuteron energy [11]. The increase in the yield of 15.1-MeV gamma rays measured at 90° is even greater compared with the yield for the ^{11}B(d, n)^{12}C reaction. A summary of the yields of 4.4- and 15.1-MeV gamma rays yield is given in Tables III and IV, with the corresponding values plotted in Figs. 8 and 9, respectively. The yields of 4.4- and 15.1-MeV gamma rays per steradian hundred microcouloumb are calculated by

$$Y(E) = \frac{npN_\mathrm{A}}{M} \int_{E_0}^{E_1} \frac{\sigma(E)}{T(E)}\, dE, \qquad (6)$$

where n is the number of protons, p is the enrichment of the ^{12}C sample, M is the molar mass, E is the proton energy, σ is the measured production cross section [20,31–33], and T is the tabulated stopping power [34]. The estimated yields are shown in Figs. 8 and 9 assuming 20% uncertainty. The gamma-ray yields are calculated by integration from the incident energy of the proton to the reaction threshold of its respective gamma-ray energy. There is good agreement between the measured gamma-ray yields at 4.4 and 15.1 MeV and previous findings [31–33]. The differences between our experimental results and calculated yields based on previously reported cross sections

TABLE V. Results of TLD measurements over a measurement time of 8 h.

Proton energy (MeV)	Angle (deg)	TLD-700	TLD-600	
		Q_7 (nC)	Q_6 (nC)	$Q_{6,n}$ (nC)
19.5	0	8447 ± 383	8731 ± 1661	930 ± 1698
	90	8146 ± 889	9612 ± 2024	2090 ± 2184
25	0	$22\,331 \pm 4520$	$38\,724 \pm 2384$	$18\,118 \pm 4811$
	90	$19\,810 \pm 927$	$34\,400 \pm 4902$	$16\,105 \pm 4977$
30	0	$35\,722 \pm 1510$	$151\,812 \pm 9721$	$118\,822 \pm 9821$
	90	$33\,535 \pm 1870$	$117\,670 \pm 6188$	$86\,700 \pm 6424$

TABLE VI.   Estimated photon-dose and neutron-dose distributions from TLD measurements.

Proton energy (MeV)	Angle (deg)	Photon dose (μGy μC^{-1})	Neutron-dose equivalent (μSv μC^{-1})
19.5	0	13.69 ± 0.62	15.83 ± 28.92
	90	13.19 ± 1.44	35.77 ± 37.18
25	0	42.21 ± 8.56	359.83 ± 95.56
	90	37.45 ± 1.76	319.83 ± 98.85
30	0	61.39 ± 2.6	2145.27 ± 195.04
	90	45.66 ± 2.53	1565.31 ± 127.58

may be due to the lack of fine-resolution cross-section data and our assumption of isotropic angular distributions.

The threshold for neutron production in the ^{12}C(p,n) reaction is 19.64 MeV [22]. Neutrons can also be produced below this threshold, for example from isotopic impurities such as ^{13}C in the target and from energetic gamma rays produced in the target and interacting in the surrounding material. The presence of fast neutrons is confirmed in Fig. 3, where the proton energy is below the ^{12}C(p,n) threshold. The results indicate that as the energy of the protons is increased, the endpoint of the light-output distribution corresponding to neutrons increases, and therefore there is also an increasing trend in the energy of neurons produced. We also observe an increase in the total number of neutrons produced with increasing incident proton energy.

The photon-dose and neutron-dose equivalents can be obtained from the measured total readings Q_7 and Q_6 of the TLD-700 and TLD-600 chips and are shown in Table V. Each reading is averaged from the results obtained with three independent chips, and the uncertainty is quoted as the associated standard deviation. Because the photon flux is larger than the neutron flux in the experimental environment and the TLD-700 chip is much less sensitive to neutrons than the TLD-600 chip (for neutron energy of approximately 10 MeV or less) [28], the total readings Q_7 of the TLD-700 chip are dominated by the photon response, such as $Q_7 \simeq Q_{7,p}$. Therefore, the photon dose given in Table VI is estimated from Eq. (2) and the 8-h measurement time. Following the calculation using Eqs. (3) and (4), the neutron response $Q_{6,n}$ of the TLD-600 chip can be estimated, and is given in Table V.

When $E_p = 19.5$ MeV, the TLD-600 results indicate that the neutron flux is much lower than the photon flux, so the neutron reading $Q_{6,n}$ represents a minor component of the Q_6 response. This low neutron flux is near the detection limit of the TLD-600 chip, resulting in significant uncertainties in the measured Q_6 and the estimated $Q_{6,n}$. When the proton energy E_p is increased to 25 and 30 MeV, the Q_7 and Q_6 readings also increase as a result of the increased photon and neutron flux. For the TLD-600 chip, the neutron reading $Q_{6,n}$ becomes comparable to the corresponding photon reading $Q_{6,p} = Q_6 - Q_{6,n}$ for $E_p = 25$ MeV, while $Q_{6,n}$ can greatly surpass $Q_{6,p}$ for

$E_p = 30$ MeV. The neutron-dose equivalent in Table VI is evaluated with Eq. (5). The TLD data in Tables V and VI indicate a 2 orders of magnitude increase of the neutron-dose equivalent at 0° when the proton energy is increased from 19.5 to 30 MeV; a moderate fivefold enhancement is obtained for the photon dose over the same proton-energy range.

V. CONCLUSIONS

Shipping manifests reported in Ref. [35] show that containers containing high-Z material account for less than 0.01% of cargo. The detection criteria for a high-Z-based active-interrogation system would have to be carefully selected to ensure an acceptable false-positive rate. A practical system could incorporate a combination of photon and/or neutron radiographic signatures [9] as well as fission signatures such as delayed neutrons [14] to maximize the probability of detection. A comprehensive study is recommended to develop a detailed design and concept of operations for such a system, but is beyond the scope of this paper.

Modest-size cyclotrons capable of accelerating protons to 25 MeV with currents of up to 400 μA are readily available [36], and even-more-compact designs with currents of up to 1 μA are under development [37]. Although it is not portable, the cyclotron described in Ref. [36] could still be installed at a fixed location such as a port of entry. This cyclotron's magnet is 3 m in diameter and weighs 30 tons; its radio-frequency system requires 25 kW for operation. These SWAP (size, weight, and power) parameters are modest in comparison with standard shipyard cranes in both power and weight.

The measured current-normalized thick-target 4.4- and 15.1-MeV-gamma-ray yields from the ^{12}C(p, p')^{12}C reaction at both 0° and 90° are greater than the previously measured ^{11}B(d,γn)^{12}C 0° yield at an incident deuteron energy of 3-MeV for all proton energies studied. The highest 15.1-MeV-photon yield was measured at a proton energy of 30 MeV at 90°, and represents an approximately 70-fold increase over the ^{11}B(d, γn)^{12}C reaction at 0° at a deuteron energy of 3 MeV. The photon dose measurements show increases in photon dose that are nearly
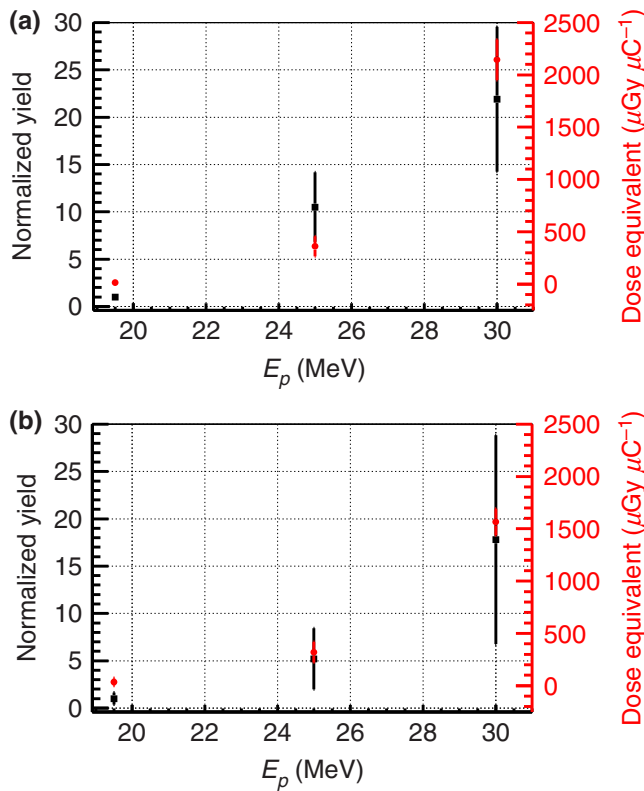
FIG. 10. Yield of 15.1-MeV gamma rays normalized to the yield at E_p = 19.5 MeV and neutron-dose equivalent for incident proton energies of 19.5, 25, and 30 MeV. Results from EJ-309 detectors and TLDs are shown at (a) 0° and (b) 90°.

commensurate with the increase in the measured 4.4-MeV-gamma-ray yield as the proton energy is increased. Figure 10 shows the gamma-ray yield normalized to the yield at E_p = 19.5 MeV and the neutron dose at three proton energies used in the experiment. Unlike the photon dose, the neutron dose increases at a rate much greater than the 15.1-MeV-photon yield as the proton energy is increased in the range from 19.5 to 30 MeV. There is a 2 orders of magnitude increase of the neutron dose when the proton energy is raised from 19.5 to 30 MeV, while an approximately fivefold increase is observed for the photon dose over the same proton energy range. Increasing the proton energy to 30 MeV results in increases of gamma-ray yields, but these are outpaced by the increases in neutron dose.

The ^{12}C(p, p')^{12}C reaction source could potentially address some of the key technical specifications required for new active-interrogation systems [8]. By taking advantage of the emission of gamma rays into a large solid angle, even multiple cargo scanning streams may be feasible with a single source, thereby increasing the container throughput. With no direct neutron production at proton energies below 19.5 MeV, the ^{12}C(p, p')^{12}C reaction should further reduce the neutron-shielding requirements and lower the total radiation dose imparted to cargo or

stowaways [16]. The reduction in the amount of required shielding would also reduce the overall geometric footprint—another important consideration in system development. The gamma-ray energies produced by this reaction would provide higher penetration capability than existing bremsstrahlung systems (photon-energy endpoints of 6 and 9 MeV) while enabling robust material discrimination by means of dual-energy photon radiography [11,12].

[1] R. Kouzes, Detecting illicit nuclear materials: The installation of radiological monitoring equipment in the united states and overseas is helping thwart nuclear terrorism, Am. Sci. **93**, 422 (2005).

[2] R. Runkle, L. Smith, and A. Peurrung, The photon haystack and emerging radiation detection technology, J. Appl. Phys. **106**, 7 (2009).

[3] C. Grassley, M. Baucus, B. Thomas, and C. Rangel, in *General Accounting Office, US Congress, GAO-03-770* (2003).

[4] M. Thibault, M. Brooks, and K. Button, The response of the us maritime industry to the new container security initiatives, Transp. J. **45**, 5 (2006).

[5] I. Jovanovic, and A. Erickson, *Active Interrogation in Nuclear Security: Science, Technology and Systems* (Springer, Switzerland, 2018).

[6] C. Geddes, B. Ludewigt, J. Valentine, B. Quiter, M.-A. Descalle, G. Warren, M. Kinlaw, S. Thompson, D. Chichester, C. Miller, *et al.*, Impact of monoenergetic photon sources on nonproliferation applications final report, Tech. Rep. (Idaho National Lab.(INL), Idaho Falls, ID (United States), 2017).

[7] J. Jones, J. Sterbentz, W. Yoon, and D. Norman, in *AIP Conference Proceedings* (AIP, 2009), Vol. 1194, p. 43.

[8] W. C. Organization, Guidelines for the procurement and deployment of scanning/NII equipment, Tech. Rep. (2015).

[9] J. Nattress, Ph.D. thesis, University of Michigan, 2018.

[10] T. Taddeucci, R. Sheffield, T. Massey, D. Carter, J. O'Donnell, C. Brune, D. Ingram, D. Jacombs, and A. DiLullo, Neutron and Gamma-Ray Production with Low-Energy Beams, Los Alamos National Laboratories Report LA-UR-07-2724 (2007).

[11] P. Rose, A. Erickson, M. Mayer, J. Nattress, and I. Jovanovic, Uncovering special nuclear materials by low-energy nuclear reaction imaging, Sci. Rep. **6**, 24388 (2016).

[12] B. Henderson, H. Lee, T. MacDonald, R. Nelson, and A. Danagoulian, Experimental demonstration of multiple monoenergetic gamma radiography for effective atomic number identification in cargo inspection, J. Appl. Phys. **123**, 164901 (2018).

[13] J. Nattress, T. Nolan, S. McGuinness, P. Rose, A. Erickson, G. Peaslee, and I. Jovanovic, High-Contrast Material Identification by Energetic Multiparticle Spectroscopic Transmission Radiography, Phys. Rev. Appl. **11**, 044085 (2019).

[14] M. Mayer, J. Nattress, and I. Jovanovic, Detection of special nuclear material from delayed neutron emission induced by a dual-particle monoenergetic source, Appl. Phys. Lett. **108**, 264102 (2016).

[15] J. Nattress, K. Ogren, A. Foster, A. Meddeb, Z. Ounaies, and I. Jovanovic, Discriminating Uranium Isotopes Using the Time-Emission Profiles of Long-Lived Delayed Neutrons, Phys. Rev. Appl. **10**, 024049 (2018).

[16] T. Taddeucci, High-energy gamma rays from ^{1}2C(p,p'), Tech. Rep. (Los Alamos National Lab.(LANL), Los Alamos, NM (United States), 2011).

[17] M. Chadwick, P. Oblozinskỳ, M. Herman, N. Greene, R. McKnight, D. Smith, P. Young, R. MacFarlane, G. Hale, S. Frankle, and et al., ENDF/B-VII. 0: Next generation evaluated nuclear data library for nuclear science and technology, Nucl. Data Sheets **107**, 2931 (2006).

[18] F. Ajzenberg-Selove, Energy levels of light nuclei $a = 11$–12, Nucl. Phys. A **506**, 1 (1990).

[19] E. K. Warburton, and H. O. Funsten, High-energy gamma rays and low-energy protons and deuterons from C^{12} + p for $E_p = 14$–20 MeV, Phys. Rev. **128**, 1810 (1962).

[20] D. Measday, P. Fisher, A. Kalmykov, F. Nikolaev, and A. Clegg, The $^{12}C(p, p')^{12}C$ (12.71 and 15.11 MeV) reaction from threshold to 50 MeV, Nucl. Phys. **45**, 98 (1963).

[21] R. H. Howell, F. S. Dietrich, D. W. Heikkinen, and F. Petrovich, (p,p') spin-flip measurement for 1^+ states in ^{12}C at $E_p = 23.5$–27 MeV, Phys. Rev. C **21**, 1153 (1980).

[22] E. Rimmer, and P. Fisher, Resonances in the (p,n) reaction on ^{12}C, Nucl. Phys. A **108**, 561 (1968).

[23] D. Berghofer, M. Hasinoff, R. Helmer, S. Lim, D. Measday, and K. Ebisawa, High-energy levels in ^{1}3N (II), Nucl. Phys. A **263**, 109 (1976).

[24] J. Nattress, and I. Jovanovic, Response and calibration of organic scintillators for gamma-ray spectroscopy up to 15-MeV range, Nucl. Instrum. Methods Phys. Res., Sect. A **871**, 1 (2017).

[25] Eljen Technologies: Neutron/Gamma PSD Liquid Scintillator Data Sheet EJ-301, EJ-309, (retrieved April 22, 2017).

[26] CoMPASS User Manual UM5960 (2018).

[27] G. F. Knoll, *Radiation Detection and Measurement* (Wiley, Hoboken, NJ, 2010), 4th ed.

[28] F. Hsu, M. Chiu, Y. Chang, C. Yu, and H. Liu, Estimation of photon and neutron dose distributions in the THOR BNCT treatment room using dual TLD method, Radiat. Meas. **43**, 1089 (2008).

[29] S. Agostinelli et a*l.*, Geant4—A simulation toolkit, Nucl. Instrum. Methods Phys. Res., Sect. A **506**, 250 (2003).

[30] R. Brun, and F. Rademakers, ROOT—An object oriented data analysis framework, Nucl. Instrum. Methods Phys. Res., Sect. AA **389**, 81 (1997).

[31] P. Dyer, D. Bodansky, A. Seamster, E. B. Norman, and D. Maxson, Cross sections relevant to gamma-ray astronomy: Proton induced reactions, Phys. Rev. C **23**, 1865 (1981).

[32] K. T. Lesko, E. Norman, R.-M. Larimer, S. Kuhn, D. Meekhof, S. Crane, and H. Bussell, Measurements of cross sections relevant to γ-ray line astronomy, Phys. Rev. C **37**, 1808 (1988).

[33] F. Lang, C. Werntz, C. Crannell, J. I. Trombka, and C. Chang, Cross sections for production of the 15.10 MeV and other astrophysically significant gamma-ray lines through excitation and spallation of C12 and O16 with protons, Phys. Rev. C **35**, 1214 (1987).

[34] M. J. Berger, J. S. Coursey, and M. A. Zucker, ESTAR, PSTAR, and ASTAR: Computer Programs for Calculating Stopping-Power and Range Tables for Electrons, Protons, and Helium Ions (version 1.2.3).

[35] M. Descalle, D. Manatt, and D. Slaughter, Analysis of recent manifests for goods imported through US ports, Tech. Rep. (Lawrence Livermore National Lab. (LLNL), Livermore, CA (United States), 2006).

[36] Best Cyclotron Systems, Best 25p Cyclotron Data Sheet (retrieved April 21, 2020).

[37] C. Johnstone, R. Agustsson, S. Boucher, S. Kutsaev, A. Smirnov, and R. Lanza, in *22nd International Conference on Cyclotrons and their Applications* (JACoW Publishing, 2019), p. 224.